Parametric investigations of the induced shear stress by a laser generated bubble

Phoevos Koukouvinis[1,], George Strotos[2], Qingyun Zeng[3], Roberto Gonzalez-Avila[3], Andreas Theodorakakos[4], Manolis Gavaises[1], Claus-Dieter Ohl[5]*

1. City, University of London, Northampton Square, London EC1V 0HB, United Kingdom
2. Technological Educational Institute of Thessaly, Mechanical Engineering Department, 41110 Larissa, Greece
3. Division of Physics and Applied Physics, School of Physical and Mathematical Sciences, Nanyang Technological University, 21 Nanyang Link, Singapore 637371
4. Technological Educational Institute of Piraeus, Mechanical Engineering Department, Thivon 250, Egaleo 122 41, Greece
5. Institute of Experimental Physics, Soft Matter Department, Otto von Guericke University Magdeburg, Universitätsplatz 2, D-39106 Magdeburg

(*) Corresponding author, email: foivos.koukouvinis.1city.ac.uk

Keywords: Numerical simulation, compressible bubble dynamics, bubble collapse, shear stress, surface cleaning.

Abstract. The present paper focuses on the simulation of the growth and collapse of a bubble in the vicinity of a wall. Both liquid and gas phases are assumed compressible and their interaction is handled with the Volume Of Fluid (VOF) method. The main interest is to quantify the influence of the induced shear stress and pressure pulse in the vicinity of the wall, for a variety of bubble sizes and bubble wall distances. Results are validated against prior experimental results, such as measurements of the bubble size, induced pressure field and shear stress on the wall. Simulation predictions indicate that the wall in the vicinity of the bubble is subjected both to high shear stresses and large pressure pulses, due to the growth and collapse of the bubble. In fact, pressure levels of 10bar or more and shear stresses up to 15kPa have been found at localized spots on the wall surface, at the region around the bubble. Moreover, the simulations are capable of providing additional insight to the experimental investigation, since the inherent limitations of the latter are avoided. The present work may be considered as a preliminary investigation in optimizing bubble energy and wall generation distance for ultrasound cleaning applications.

1. Introduction

Ultrasound cavitation applications (known also as sonochemical applications) have extended use in biomedical and industrial fields [1]. Undeniably, the cutting edge of such applications involves surface cleaning [2-4], material processing [5], in vivo treatment of various conditions (mentioning here as a non-exhaustive reference, kidney stone lithotripsy [6], cancer cell histotripsy [7]), cell sonoporation [8], drug or even DNA [9] delivery, micro-streaming [10] etc. The operating principle is based on forced bubble oscillation due to external acoustic fields.

The case of surface cleaning has gained popularity lately, since it is considered an attractive alternative to using potentially harmful detergents. This applies both in the case of domestic applications, e.g. ultrasound washing machines, and to high-tech industry, e.g. in computer chip and semiconductor manufacturing industries where organic impurities are removed with very aggressive oxidizers [11]. Additional advantages of cavitation surface cleaning include micro-jetting penetrating in

surface crevices [12], thus achieving deep cleaning and contaminant removal. The violent collapse of bubbles is known to produce high temperatures and pressures, resulting to chemical reactions (hence the name sonochemical) and the production of free radicals [13,14]. These free radicals can further enhance cleaning capacity, by neutralizing harmful substances or microbes.

Despite the potential of ultrasound applications and the advances in physical understanding of the microscale (selectively [15,16]), progress at macroscale prediction of ultrasound cavitation and its effects has been slow and mainly from the experimental side (selectively [2,3,14]), due to the complexity and the vast disparity of scales of the underlying phenomena. In particular, the bubble spatial scale is on the order of micrometers, whereas the cleaned surface dimensions may be in the order of centimetres or decimetres. The temporal scale of bubbles may be around microseconds, whereas cleaning takes place in the course of minutes if not hours.

Research on the field of ultrasound cleaning is done using either numerical or experimental techniques. On the numerical side, there are many works on the interaction of bubbles with rigid or deforming boundaries. Undoubtedly, one of the most influential and pioneering works on the field of bubble/wall interaction is the one by Plesset et al. [17], who simulated the collapse of an initially spherical bubble using the Marker-and-Cell method, demonstrating the micro-jet formation. Over the time, alternative methodologies have been employed in tracking non-spherical bubble dynamics. Examples are the Boundary Element Method (BEM), which is commonly used in simulations aiming to achieve a high quality representation of the bubble shape, though it is somewhat limited in handling topological changes of the bubble interface[18]. Indicative works include interaction of bubbles with free surfaces and/or walls [19], bubble growth [20] and multi-level simulations of bubble dynamics, involving coupling of solids/fluids and compressible/incompressible approaches [21]. Apart from the BEM method, alternative techniques involved the integration of 2D/3D Navier-Stokes equations using interface tracking techniques [22] or interface capturing techniques, such as Level-Set [23] and Volume-of-Fluid (VOF) [24-26]. In the field of surface cleaning, the only existing contribution of numerical study, is the work of Chahine et al. [15] where the authors tracked the interaction of a collapsing bubble with a cube-shaped object, which was assumed to be a dirt particle, demonstrating a strong flow field which can dislodge attached contaminants from surfaces. Before closing this section, it is highlighted that, whereas in many computational studies a common simplification for tracking cavitation is to employ the Rayleigh-Plesset equation, such an approach is only applicable to spherical bubbles [27], thus it cannot adequately describe the asymmetries imposed by pressure gradients.

On the experimental side, there are several works discussing the cleaning effect of cavitation. Among them, Rivas et al. [2] studied the manipulation of acoustic nucleation by introducing roughness elements at selected locations on the cavitating surface. On a similar subject, Bremond et al. [16,28] studied the evolution of bubbles formed at clusters of roughness elements, extending the Rayleigh-Plesset equation modelling, by taking into account bubble to bubble interactions. Furthermore, in [3], Rivas et al. have exploited the controlled cavitation formation to achieve surface cleaning of surfaces coated with polymers, metals, etc. thus paving the path to efficient techniques for ultrasound cleaning. Reuter et al. [29] discussed the application of ultrasound cavitation in membrane cleaning, correlating the dependence of the membrane sheet distance and arrangement to the cleaning results, quantified in terms of material dirt removal. Further works by the same authors [30,31] focused more on the dependence of the cleaning capacity of ultrasound cavitation on ultrasound characteristics, such as frequency and excitation driving power. The listed works so far involved more applied cases, with little discussion on fundamental aspects of the flow. On the fundamental side, the only work we are aware of is that of Dijking et al. [32,33], who employed a Constant Temperature Anemometry (CTA) transducer to measure the shear stress induced by the growth and collapse of laser generated bubbles, while also recording the pressure signal with hydrophone and bubble size with a high speed camera.

Despite the existence of several works on bubble evolution near boundaries, there are limited works discussing the induced shear by collapsing bubbles. From the numerical side, only Chahine et al. attempted to track the interaction of bubbles with dirt particles, in an idealised and non-validated case [15]. From the experimental side, only the work of Dijkink et al. [32] measured bubble induced shear stresses due to micro-jet interaction with nearby walls. Even in this case, there have been experimental limitations, that prevented a thorough analysis of the physical mechanisms taking place. In particular, the spatial and temporal scale of the macroscopic phenomenon under consideration was in the order of 0.7mm and 0.1ms respectively; note that these scales correspond to the maximum bubble radius and one bubble expansion/collapse cycle. It has to be kept in mind though that these are the maximum possible scales, since characteristic flow features may occur at much smaller scales; for example the developing jet has a radius of 0.1mm and jet spreading occurs within 50μs. These scales are at the borderline of measuring capability of modern equipment, rendering visualization and experimentation difficult. Apart from problematic high-speed imaging, it was reported that the measurement surface of the shear stress sensor was comparable to the size of the bubble and that shear stress measurements were limited by the sensor bandwidth [32]. Thus, our aim in the present work is to extend the aforementioned investigation, employing Computational Fluid Dynamics, to demonstrate the capability of predicting bubble-induced shear stresses and demonstrating the fundamental flow mechanisms. In this way, many limitations of the experimental techniques are avoided, since the flow field is directly accessible. The present work can be then further used for the prediction of bubble wall interactions aiming towards a better understanding of surface cleaning applications.

The present paper is organised as follows: section 2 discusses the numerical methodology, section 3 the case set-up and justifies the conditions and models used, section 4 is a validation of the numerical model against published data [32] including shear stress, pressure signal and discussion on physical mechanisms. Following, in section 5, there are parametric investigations for different bubble configurations, such as smaller/larger bubble to wall distance or different bubble energies. The results are discussed and conclusions are presented in section 6.

2. Numerical model

The numerical model that was used for the CFD simulations is based on the Volume Of Fluid (VOF) method, since it is of interest to maintain a sharp interface between the two involved phases, with topological changes of the interface. As mentioned, only water and gas are considered, whereas vapour presence and mass transfer effects are ignored. The justification of this assumption is the fast process of bubble growth and collapse that means there is little time available for effective mass transfer.

Continuity and momentum equations are solved, while thermal effects are ignored. The equations solved, based on the viscous form of the Navier-Stokes equations, (for more information, the interested reader is addressed to standard CFD textbooks, such as [34-37]), are as follows:

- Continuity equation:

$$\frac{\partial \rho}{\partial t} + \nabla \cdot (\rho \mathbf{u}) = 0 \tag{1}$$

where $\mathbf{u}$ denotes the velocity vector of the flow field.

- Momentum equation:

$$\frac{\partial \rho \mathbf{u}}{\partial t} + \nabla \cdot (\rho \mathbf{u} \otimes \mathbf{u}) = -\nabla p + \nabla \cdot \boldsymbol{\tau} + \rho \mathbf{g} + \mathbf{f} \tag{2}$$

where ρ is the density of the fluid, p is the pressure, $\mathbf{g}$ is the gravity vector, $\mathbf{f}$ are body forces and $\boldsymbol{\tau}$ is the stress tensor, defined as follows:

$$\boldsymbol{\tau} = \mu \left[\nabla \mathbf{u} + (\nabla \mathbf{u})^T \right] + \lambda (\nabla \cdot \mathbf{u}) \mathbf{I} \tag{3}$$

In eq. 4, **I** is the identity matrix and μ is the dynamic viscosity of the fluid; for the pure phases it is set to 1mPa·s and 17.1μPa·s for water and air accordingly. The term λ denotes bulk viscosity of the fluid which acts only on passing waves [38]. Its effect is more relevant to sound wave propagation [39] and thus has been omitted in the present study. The maximum Reynolds number of the flow ranges around 10000 or less, for the majority of the simulation time, so turbulence modelling has not been used.

Surface tension effects are included, employing the Continuum Surface Force Model which represents surface tension as a volume force in cells where there is an interface, i.e. volume fraction varies from zero to unity, see Brackbill [40]. The value for surface tension coefficient used is σ=0.072N/m. In any case, surface tension effects are considered minor, given an indicative Weber number of ~7000 for the jet inside the bubble.

- Volume fraction equation [41]:

$$\frac{\partial a\rho_g}{\partial t} + \nabla \cdot \left(a\rho_g \mathbf{u}\right) = 0 \tag{4}$$

where a represents the volume fraction and ρ_g the density of the gas phase. In the interface, where a varies from zero to unity, volume fraction averaging is performed for determining the value of viscosity and density.

Whereas in the actual experiment there is significant influence of heating effects, due to laser interaction with the liquid, the resulting fluid state is not possible to describe with traditional equation of states, such as ideal gas or other, since plasma generation and chemical reactions may take place. For this reason some simplifications had to be made and the energy equation has been omitted, since it is redundant in the thermodynamic closure chosen. Even with the omission of thermal effects, both phases are assumed compressible, obeying the following equations of state:

- for the liquid, the Tait equation of state:

$$p = \frac{\rho_0 {c_0}^2}{n_l}\left(\left(\frac{\rho}{\rho_0}\right)^{n_l} - 1\right) + p_0 \tag{5}$$

where, ρ_0 is liquid density, equal to 998.2kg/m^3, c_0 the speed of sound, equal to 1450m/s, at the reference state p_0=3490Pa. The exponent n_l is set to 7.15, according to relevant literature on weakly compressible liquids, such as water [42]. Choice of the Tait equation of state is justified considering that it matches closely the IAPWS liquid water data [43], comparing to simple linearized equations (as e.g. in [44]), especially at extreme pressures, where the deviation in predicted densities may exceed 10%.

- for the gas, a polytropic equation of state is used:

$$p = k\rho^n \tag{6}$$

Constant k is case dependent; here it is set assuming a gas density of ~1.2kg/m^3 (calculated from ideal gas for a temperature of 25^{o}C) at the ambient pressure of 101325Pa. The exponent n is set close to unity, as in the Rayleigh-Plesset equation. For both equations of state, speed of sound c is defined as follows [45]:

$$c = \sqrt{\left(dp \middle/ d\rho\right)} \tag{7}$$

Equations (2) and (3) are solved with a pressure-based algorithm, i.e. a pressure correction equation is solved. Then the pressure correction is linked to a velocity correction and to a density correction through the speed of sound (eq. 8, see also [34,46]), to satisfy mass balance of fluxes in each cell. In order minimise the effect of numerical diffusion, which could affect the development of the bubble during the whole process of growth and collapse, second order upwind schemes have been used for the discretization of density and momentum, while the VOF phase field has been discretized using a compressive differencing scheme [47] to maintain a sharp interface. Time stepping is done with an adaptive method, to achieve a Courant-Friedrichs-Lewy (CFL) condition [41] for the free surface

propagation of 0.2. This is necessary, to limit as much as possible the interface diffusion and maintain solution accuracy at near the free surface [48]. The solver used is implicit pressure-based and this removes any restrictions on the acoustic courant number, which is ~10 (on average) considering the minimum cell size and the maximum wave velocity.

3. Case description and set-up

The general configuration of the cases examined is shown in Figure 1. A bubble is generated at a distance, h, from a nearby wall surface, using a focused laser beam (λ=532 nm, pulse duration of 6 ns). The laser pulse leads to intense heating and plasma formation in the focused region. After the bubble generation, the bubble expands rapidly, due to the high pressure gas/plasma, and within a time interval of ~75μs it reaches a maximum radius of R_{max} ~ 0.7mm. When reaching the maximum bubble size, pressure inside the bubble has dropped to sub-atmospheric levels, leading to the collapse process. However, the collapse is affected by the pressure gradient induced by the wall and becomes asymmetric. In fact, the bubble side opposite to the wall collapses at a faster rate than the rest of the bubble. This leads to the well-known mirco-jet formation [49], which pierces the bubble, forming two toroidal cavities. After piercing the bubble, the micro-jet has enough momentum to continue towards the wall, eventually impinging on the wall surface and forming a shear layer in the wall vicinity, which is further enhanced by the rebound (i.e. expansion) of the collapsed bubble. The bubble itself, dragged by the flow, moves closer to the wall as it is expanding. Thus, later on, after its expansion, the bubble collapses again, generating additional shearing.

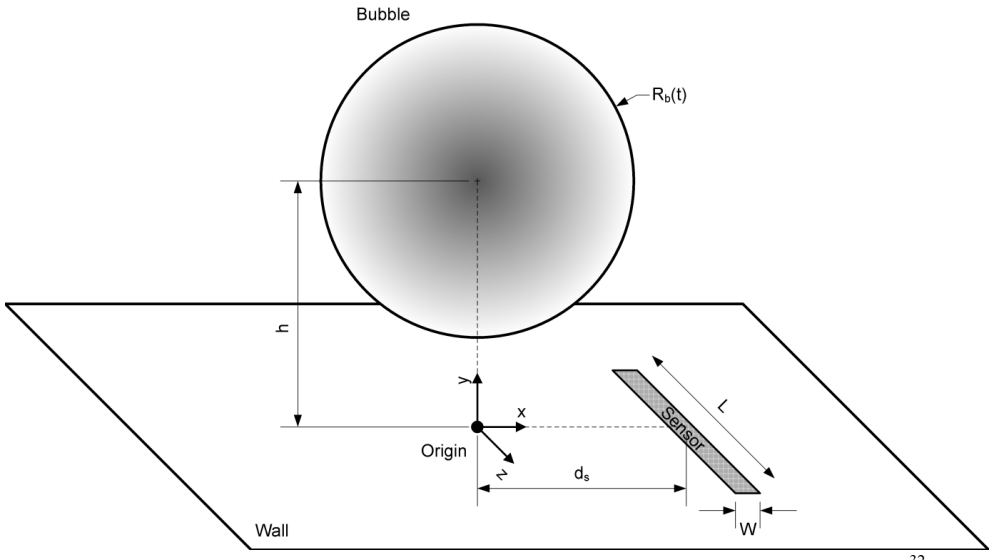

Figure 1. General bubble arrangement for bubble collapse induced shear measurements, see [32].

The whole experiment was conducted in a rectangular liquid container of dimensions 80×80×80 (W×H×L, in mm), filled up to 25mm with water, while bubbles were generated at a distance of ~0.8mm from the bottom wall, at the centre of the container. In the experiment [32], shear stress is measured by a sensor of finite dimensions, placed at a distance, d_s, from the projected bubble centre on the wall. The sensor has dimensions of 0.2 × 0.75 mm (W × L) and in the experiment it was placed at d_s=0.25mm. Simulations, on the other hand, provide shear stress at discrete points, thus to get a comparable result as the experiment, shear stress averaging is performed over the area that is covered by the sensor. By considering the configuration of Figure 1, it becomes apparent that the maximum bubble size is comparable to the sensor size. However, it is highlighted that the bubble size varies in time, due to gas expansion/collapse. In order to obtain a similar effect in simulations, a spherical

nuclei of gas, of initial radius R_0, is patched in a pure liquid domain, at a high pressure p_{g0}; the methodology of determination or R_0 and p_{g0} is explained later on in the present section.

Since other boundaries are at relatively large distances (40mm, or ~57 non-dimensionalized by the maximum bubble radius) from the bubble, the influence of the sidewalls is negligible. Thus, the bubble/wall interaction may be simplified as axis-symmetric; as shown in Figure 1, only solving a two-dimensional slice, e.g. *x-y* plane of the complete domain. In this way, the simulation is much more efficient in terms of computational time and resources needed, since a full three-dimensional simulation would involve a significantly higher computational cost, associated with the increased cell number to properly resolved the flow field in all three dimensions.

A non-dimensional analysis indicates the effect of the pressure gradient asymmetry factors, such as gravity and boundary presence. From extensive prior experimental work [50], a non-dimensional scaling law governing the collapse asymmetry and outcome, has been formulated as follows:

$$\zeta = \frac{|\nabla p| R_{\max}}{p_\infty - p_v} \tag{8}$$

where $|\nabla p|$ is the pressure gradient due to e.g. gravitational force or boundary presence, R_{max} is the maximum bubble radius, p_∞ is the pressure at cavity level and p_v is the vapour pressure. The higher the ζ value, the more pronounced the aspherical collapse. In the case of gravity, the pressure gradient is related to the acceleration of gravity, **g**, as:

$$\nabla p = \rho \mathbf{g} \tag{9}$$

where **g** is the vector of gravitational acceleration and ρ is the liquid density.
In the case of boundary presence, such as a wall, then the pressure gradient may be found as [50]:

$$\nabla p = \frac{0.2 R_{\max} (p_\infty - p_v)\mathbf{h}}{h^3} \tag{10}$$

where **h** is the vector from the bubble centre towards the nearest wall surface. For the cases to be discussed, R_{max} ~ 0.7mm, p_∞ = 101325 Pa, p_v = 2340 Pa, h ranges from 0.6 to 1 mm. Consequently, for all cases examined the ζ parameter due to gravity is $\zeta_G \sim 7.42 \cdot 10^{-5}$, whereas the ζ parameter due to boundary influence ranges between ζ_B ~ 0.11 - 0.3. The comparison of the non-dimensional ζ parameter due to gravity and due to boundary influence demonstrates the importance of the wall effect, in relation to gravity. Indeed ζ_B is, at least, 1500 times larger than ζ_G. Thus, due to the relative insignificance of gravity, its effects are omitted in all simulations to be presented.

The cases examined consist of a validation case, performed at the conditions of the experiment (see [32]) and several parametric simulations to determine the effect of various parameters, such as bubble energy (E_b) and bubble wall distance (h) to the induced shear and pressure on the wall. The methodology for setting up the initial bubble conditions is the same as in prior work by the authors [25,26]. To be more specific, the initial radius of the bubble was assumed to be ~1/100 of R_{max}, i.e. $R_0 \sim$ 7.5 μm, based on prior experimental investigations on laser-generated bubbles [51]. The initial pressure is estimated using the Rayleigh Plesset equation, expressed in the standard form as [27]:

$$\rho\left[R\ddot{R} + \frac{3}{2}\dot{R}^2\right] = p_v - p_\infty + p_{g0}\left(\frac{R_0}{R}\right)^{3n} - \frac{2\sigma}{R} - 4\mu\frac{\dot{R}}{R} \tag{11}$$

where:

- ρ is the water liquid density, 998.2kg/m^3
- R is the bubble radius, $\dot{R} = dR/dt$ and $\ddot{R} = d^2R/dt^2$
- p_v is the vapour pressure, which is ignored in the present investigations.
- p_∞ is the ambient pressure, equal to the atmospheric 101325Pa.

- p_{g0} is the initial bubble pressure, adjusted to predict a similar maximum bubble radius as the experiment.
- σ is surface tension, equal to 0.072N/m. Note that surface tension plays a minor role in the bubble shape evolution, since the phenomenon is mainly inertial. In particular, omission of surface tension leads to a change in the collapse time of less than 0.2% and change in the maximum radius of less than 0.1%. Besides, the Weber number of the bubble is ~37000 during its generation and drops to ~7000 during the micro-jet formation at bubble collapse.
- μ is the dynamic viscosity of water, i.e. 10^{-3} Pa.s
- n is a polytropic exponent, depending on the thermodynamic process inside the bubble, e.g. for adiabatic it is equal to the heat capacity ratio and for isothermal it is unity. In this study a value close to unity has been used, since it matches better the experimental data. This is related to the small size of the bubble and may be quantified based on the bubble Peclet number, Pe, [52,53], as follows:

$$Pe = \frac{\tau_{diff}}{\tau_{dyn}} \tag{12}$$

$$\tau_{diff} = \frac{R^2}{x_g} \tag{13}$$

$$x_g = \frac{k_g}{\rho_g c_{p,g}} \tag{14}$$

where: τ_{dyn} is the dynamic timescale of bubble growth/collapse, τ_{diff} is the thermal diffusion timescale, related to the bubble radius R and the gas thermal diffusivity x_g. Gas thermal diffusivity is related to the gas thermal conductivity k_g , gas density ρ_g and gas heat capacity $c_{p,g}$. It becomes apparent that since the bubble characteristics (radius, density, etc.) change over time, due to the large variations in size, the bubble Peclet number also varies. Considering the cases to be examined here (gas values are obtained from NIST Refprop [54]):
- τ_{dyn} ~ 300μs, is the duration of the phenomenon
- the bubble radius, R, varies from 7.5 to ~700μm
- gas density, ρ_g, varies between ~1000 to 0.1kg/m^3
- heat capacity, c_p, from ~1600 to 1000J/kg·K
- thermal conductivity, k_g, from 0.71 to 0.024W/m·K

thus the bubble Peclet number varies between 0.37 and 9, indicating the strong influence of heat transfer and justifying the selection of a polytropic exponent close to unity. Besides, a similar effect was found at even larger bubbles in prior studies [25,26].

The Rayleigh-Plesset equation (eq. 11) was used to obtain a quick estimate of the initial bubble pressure, as in [25,26]. Of course, this estimate is not perfectly accurate, since the assumption of spherical symmetry, inherent in the classic Rayleigh-Plesset equation, is no longer applicable due to the wall presence. Thus, a correction step is needed, by solving the Navier-Stokes equations, as described in section 2, in the actual geometry with the wall presence. The benefit of this combined approach is the quick estimation of the initial bubble pressure p_{g0}, since only one evaluation of the more accurate Navier-Stokes solver is required, to determine the correction factor; after that, the Rayleigh-Plesset solution is much more reliable in predicting the actual bubble size.

The examined cases involve one validation case in comparison with published experimental data [32] and several parametric simulations examining the effect of the bubble-wall distance and the initial gas pressure (or max. bubble size / bubble energy) on the induced shear stress. A summary of the configurations to be discussed is outlined in the table below:

Table I. Conditions for the bubble dynamics cases examined. In all cases R_0 = 7.5μm and n = 1.025. R_{max} is estimated, assuming sphere of V_{max}.

# Case	h (mm)	p_0 (Pa)	V_{max} (mm^3)	R_{max} (mm)	E_{Rmax} (mJ)	$\tau_{Rayleigh}$ (μs)
1. validation	0.8	$8.5 \cdot 10^9$	1.3	0.681	0.12	62
2. (↓ h)	0.6	$8.5 \cdot 10^9$	1.3	0.680	0.12	62
3. (↑ h)	1.0	$8.5 \cdot 10^9$	1.3	0.684	0.12	62
4. (↓ p_0)	0.8	$2 \cdot 10^9$	0.31	0.418	0.027	38
5. (↓↓ p_0)	0.8	$5 \cdot 10^8$	0.07	0.254	0.006	23

Rayleigh time, $\tau_{Rayleigh}$, is defined as:

$$\tau_{Rayleigh} = R_{\max} \sqrt{\frac{\rho}{p_\infty - p_v}} \tag{15}$$

and bubble energy, E, as the volume of the bubble, V_b, multiplied with the average pressure difference between the farfield pressure (p_∞ = 101325Pa) and the average bubble pressure.

The computational domain is shown in Figure 2a; the domain is two-dimensional, axis-symmetric, extending from the origin up to 100mm away from the initial bubble generation site (which is more than 100 times the maximum bubble radius). In this way, bubble presence is unaffected by the pressure boundary condition. Moreover, to prevent any boundary reflections of emitted pressure waves from the bubble generation or collapse, the computational mesh is coarsened near the pressure farfield, acting as a sponge layer. The mesh is structured and split in 4 blocks, as shown in Figure 2. The mesh in zone (1), which is the area of interest, is purely Cartesian and has a uniform sizing of 2.5μm (i.e. 280 cells in the bubble radius at maximum size), to ensure accuracy and to prevent distortion of the bubble interface. The total cell count is ~ 500000 cells.

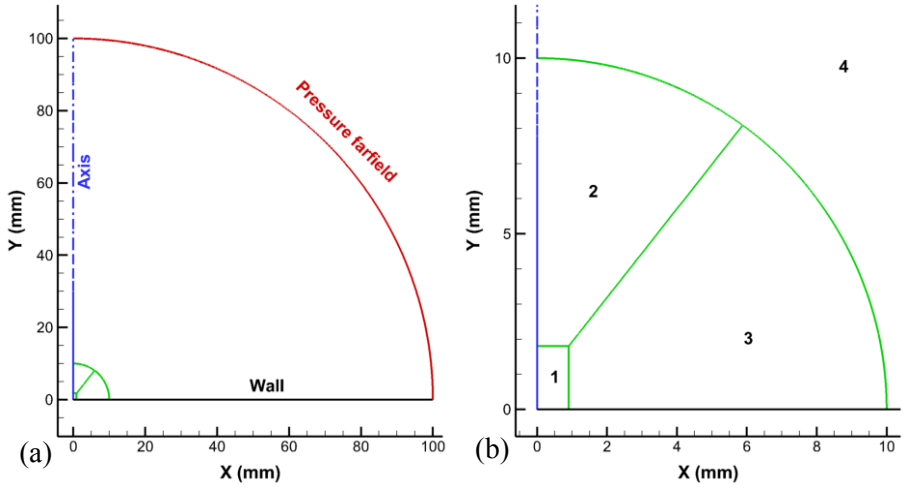

Figure 2. Mesh blocks, numbered from 1 to 4: (a) complete view, (b) magnified view new the bubble formation site. The green lines indicates the block-splitting. All blocks are structured meshes. Block 1 is Cartesian with uniform resolution of 2.5μm.

4. Validation case

As a first case to be examined is the configuration denoted with "1" in table I, which serves for validation purposes, since experimental data have been published in [32]. Results will be assessed in terms of the general flow pattern, shear stress, pressure signature (hydrophone signal), based on the initial pressure, adjusted to achieve a similar maximum bubble size.

4.1. Indicative instances

Figures Figure **3** to Figure **9** show indicative instances of the growth and collapse of the bubble, for the validation case. Each of the images is split in half by a dashed dotted line, which denotes the axis of symmetry. The left part of each figure shows the pressure field, whereas the right part the velocity magnitude. A thick black line denotes the isoline of 0.5 gas volume fraction, i.e. the bubble interface. In all cases, time is represented in absolute terms (t) and in non-dimensional form (t^*), as time divided by the Rayleigh collapse time $\tau_{Rayleigh}$ = 62μs.

At the beginning of the bubble expansion the bubble grows explosively, with interface velocities reaching even 400m/s or more, see e.g. Figure 3. Bubble interface velocity drops to less than 60m/s after 1μs of the bubble generation. At ~ 70μs, the bubble reaches its maximum radius of ~0.7mm, see Figure 3. The wall presence has an observable effect on the bubble shape, since it is no longer spherical. The bubble obtains a deformed shape, slightly compressed on the axial direction; bubble radius deviates from perfectly spherical by ~2.5%. As the bubble collapses, momentum focusing occurs at the bubble side opposite to the wall, accelerating the collapse and forming a micro-jet, see Figure 4. In short, this effect is induced by the asymmetric flow profile around the bubble, clearly shown in Figure 3 at maximum bubble size; the fluid region between the bubble and wall is at low pressures, resulting to a very low collapse velocity and a preferential collapse at the side away from the bubble. The mechanism has been extensively analyzed in previous works (e.g. selectively [49], [23], [55]) and will not be further analyzed here. The microjet radius is R_{jet} ~ 0.1mm and its velocity is u_{jet} ~ 75m/s. Later on, the jet pierces the bubble, forming a main toroidal structure, indicated with the number *1*, and smaller toroidal structures.

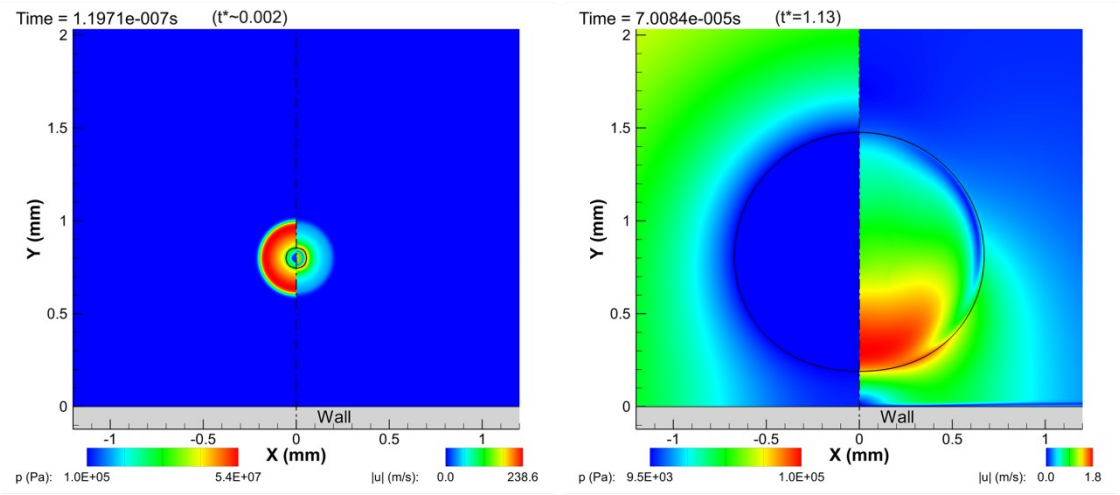

Figure 3. Left: Initial growth of the bubble. Right: maximum size of the bubble.

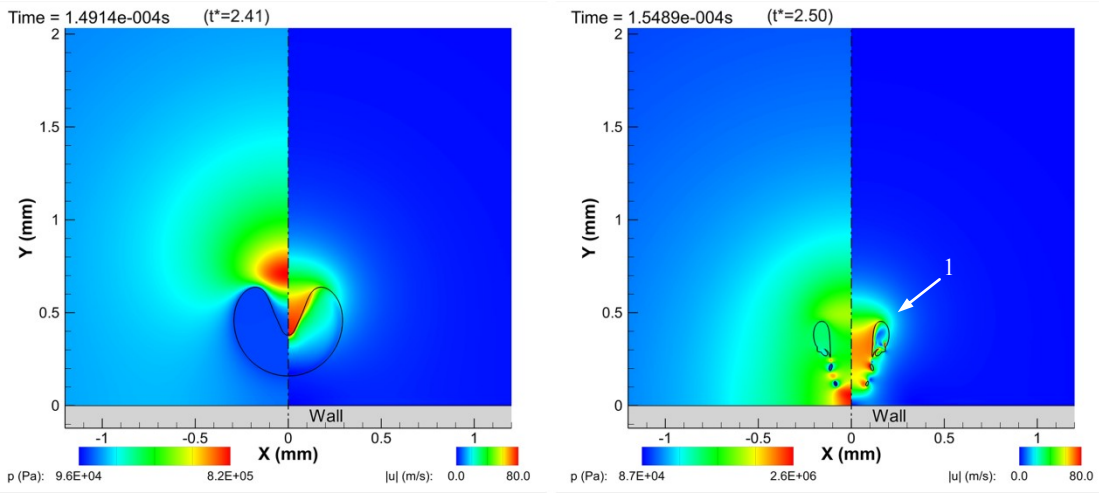

Figure 4. Left: formation of the microjet, directed towards the wall. Right: the microjet pierces the bubble, forming detached toroidal structures and impacts on the wall surface.

Later on, at 158μs, the intense shearing induced by the microjet leads to splitting of the toroidal bubble to mainly two toroidal structures, which are indicated with the numbers *1* and *2* in Figure 5. At 163μs, the rebounding process is observable and the two toroidal structures start to expand. The expansion of toroidal bubble *2* is further enhanced by the rotating motion of the liquid, due to the imparted momentum of the micro-jet. Toroidal bubble *2* is located in the core of a vortex ring of circulation ~0.02 m^2/s and a radius of ~0.12mm. It is notable that the impinged jet forms a high velocity liquid sheet on the wall surface, which causes intense shear stress, as will be demonstrated later. This liquid sheet remains attached on the wall up to 0.4mm from the axis of symmetry and then separates, see Figure 5 at 163μs. This separation point moves further away from the axis of symmetry as the toroidal bubbles expand: at 171μs (see Figure 7) the separation point moves to 0.5mm from the axis and at 215μs to 0.7mm from the axis of symmetry. Such unsteady separation patterns of impinging jets on walls have been extensively documented in prior works, e.g. [56], and are attributed to the formation of primary and secondary ring vortices. Primary ring vortices form around the jet axis whereas secondary vortices form between the expanding fluid sheet and the wall surface, leading flow detachment and giving the impression of a "rebounding effect" [57] of the liquid sheet, as shown in Figure 6.

At ~220μs the bubbly structure has expanded to peak volume after the collapse; both bubbles have a toroidal shape and are in close proximity (2.5-5μm) to the wall, or are even in contact with the wall. Bubble *2* is the smallest and appears broken (see Figure 7), due to intense shearing and flow separation. It has a minor radius of 0.15mm and a major radius of 0.77mm. Bubble 1 is much larger with a minor radius of ~0.34mm (though its shape is strongly deformed and deviates from circular) and a major radius of ~0.35mm. Note that the remnant of the micro-jet is still observable as a liquid column at the axis of symmetry.

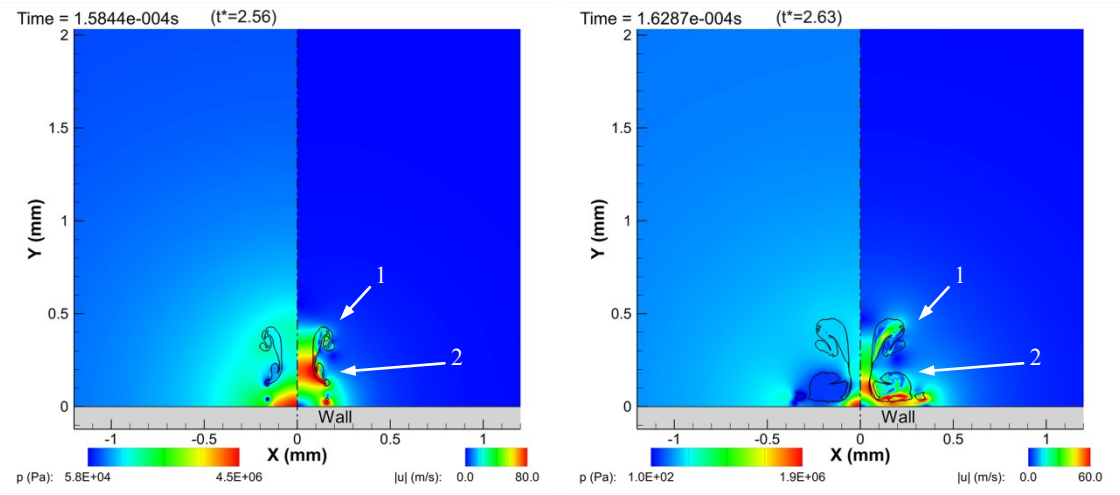

Figure 5. Left: Shearing and splitting of the main toroidal bubble. Right: during the course of the rebound process, mainly two toroidal structures remain.

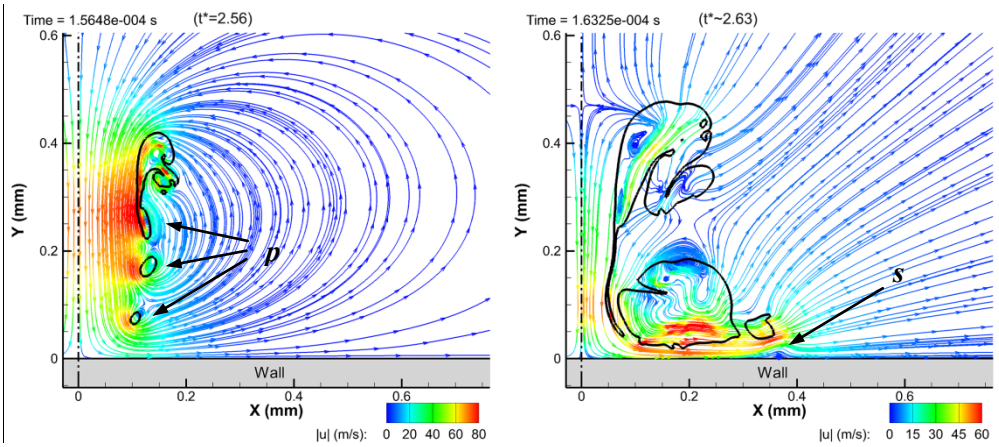

Figure 6. Demonstration of primary (*p*) and secondary (*s*) ring vortices, around the micro-jet and on the wall respectively.

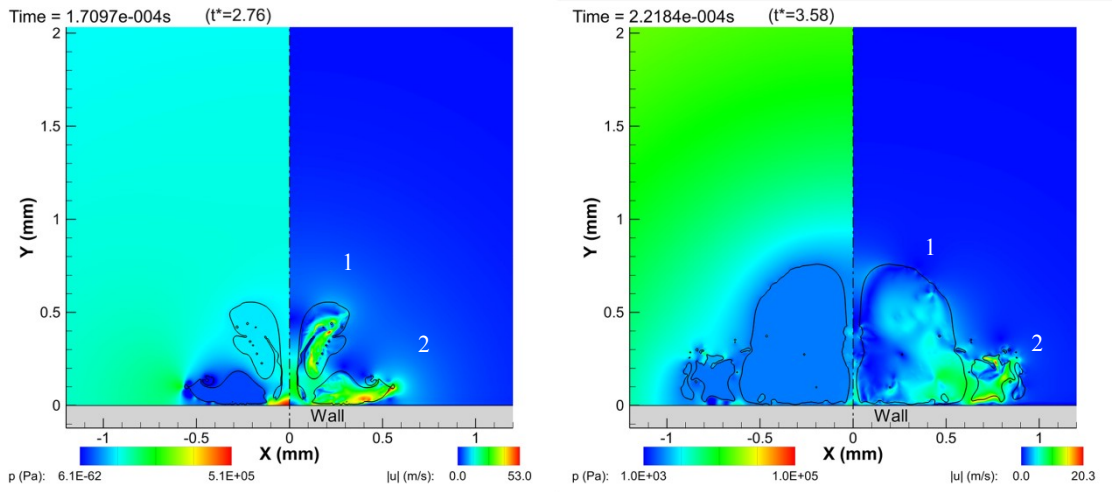

Figure 7. Left: The bubbly structures rebound and get sheared along the wall surface. Right: maximum size of the rebounding bubbly formations.

After 230μs, the two toroidal bubbles start to collapse. As shown in Figure 8, at 275μs, toroidal bubble *2* has already shrunk significantly and has broken in two smaller, irregular structures. At 306μs, bubble *2* has entirely collapsed, leaving behind only minor fragments. Later on, at 314μs in

Figure 9, toroidal bubble *1* collapses and gets compressed against the wall surface. Finally, at 325μs, the bubbly formation expands once more, but now has a highly irregular topology.

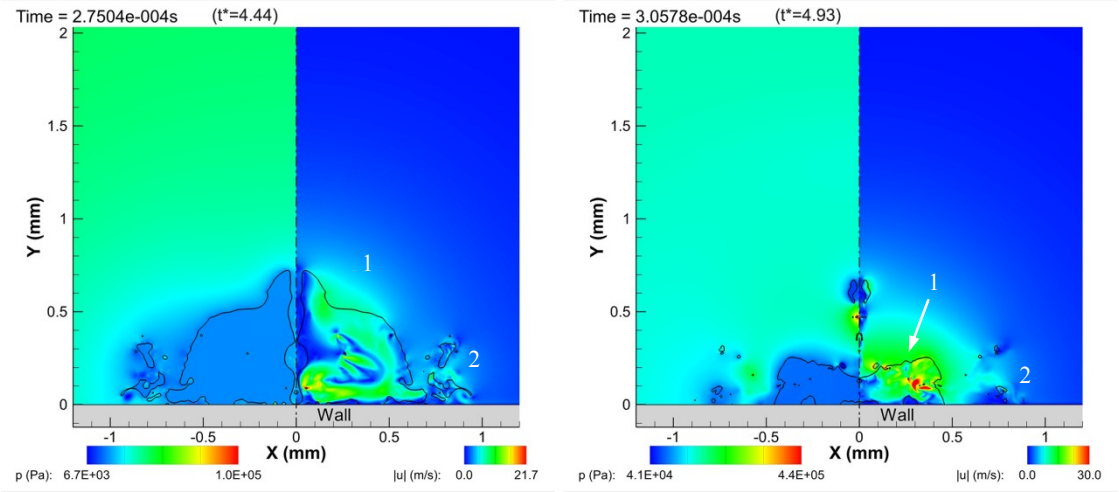

Figure 8. After the rebound, the collapse process is repeated. Toroidal structure (2) is the first to collapse.

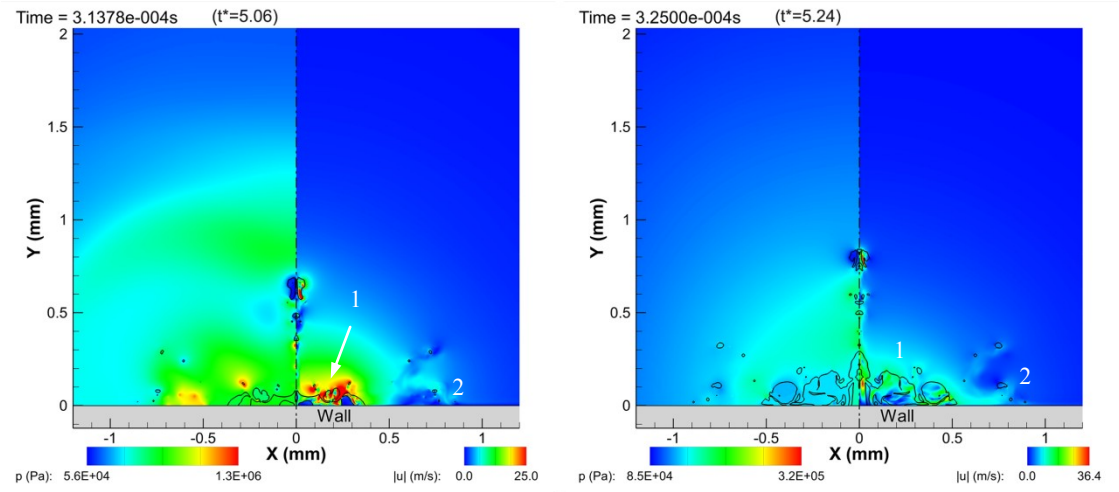

Figure 9. Left: complete collapse of the toroidal structures. Right: second rebounding cycle.

In general, the bubble generation pattern is similar to the one reported in Dijkink et al. (see supplementary material of [32]), i.e. the bubble grows up to a maximum radius of ~0.7mm at ~66μs (simulation deviation from experiment ~5%), then collapses and rebounds exhibiting an enlarged vertical structure at the middle (see Figure 10, at 165-230μs), which is similar to the toroidal bubble configuration in Figure 7. One difference with the experiment is the fact that the second collapse occurs delayed in the simulation, at 310μs instead of 253μs in the experiment. The main reason for that is the absence of a condensation mechanism, which would dampen the bubble oscillation and reduce the maximum bubble size after the rebound.

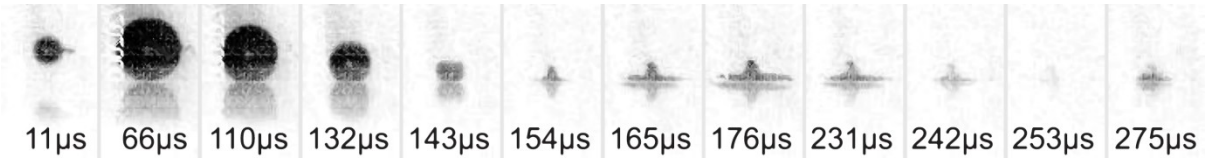

Figure 10. Sequence of images of the bubble expansion and collapse as obtained from the original experimental (see supplementary material of [32]).

4.2. Pressure wave emission and hydrophone signal

The strong accelerations and decelerations of the bubble interface create intense pressure waves that can be tracked in the simulation by performing a Schlieren visualization. The emission of pressure waves is shown in Figure 11 to Figure 13; each figure is split in half by the vertical axis of symmetry (dashed-dotted line). The left part of the figures shows the pressure field. The right part of the figures shows the Schlieren plot, based on the normalized density gradient, calculated as follows [58]:

- First, the gradient vector of the density field, $\nabla\rho$ is calculated.

- The gradient vector magnitude is used to normalize the gradient vector magnitude:

$$|\nabla\rho|' = \frac{|\nabla\rho|}{\max(|\nabla\rho|)} \tag{16}$$

- The normalized density gradient magnitude is then used to calculate the Schlieren value as:

$$Schlieren = e^{-k|\nabla\rho|'} \tag{17}$$

which is then represented in greyscale.

The explosive growth of the bubble at the initial stages after its generation cause the propagation of an expanding spherical shock wave, see *1* in Figure 11. The shock wave interacts with the wall (see *2* in Figure 11), which reflects back towards the bubble, obtaining a bow shape (see *3* in Figure 11). Later on, the reflected shock wave interacts with the bubble, reflecting once more as a rarefaction wave this time (see *4* in Figure 11).

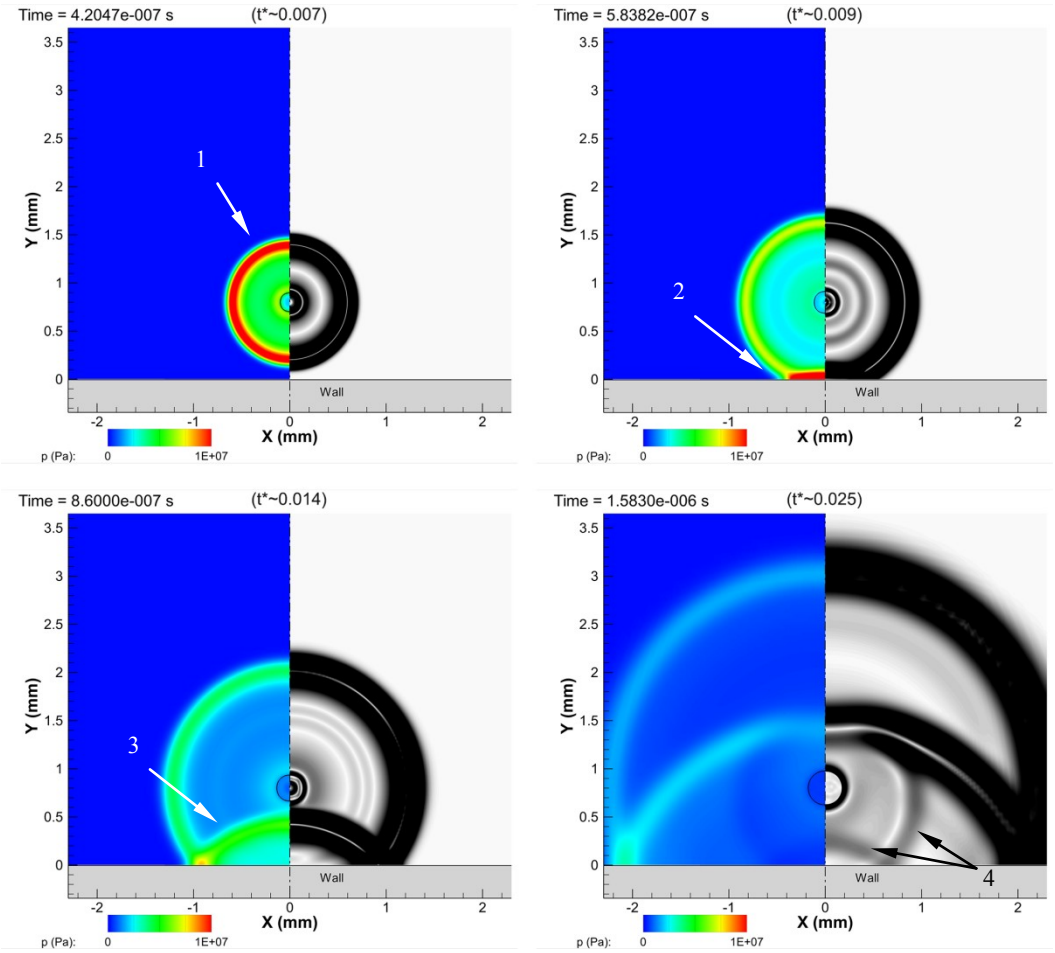

Figure 11. Left: pressure field. Right: Schlieren images during bubble growth. The bubble interface is visible as a continuous black line. The dashed-dotted line at the middle is the axis of symmetry.

Emission of shock waves is observed later on, during the first collapse of the bubble. Jet impact and piercing of the bubble generates shock waves, as well as the sudden expansion of the toroidal structures after the collapse, see *5* and *6* in Figure 12. Finally, as the main bubbly cavity gets compressed against the wall (see *1* in Figure 9) a series of shock waves is emitted, forming a rather irregular pattern, due to interaction with dispersed bubble structures in the vicinity of the collapse site (see *7, 8, 9, 10* in Figure 13).

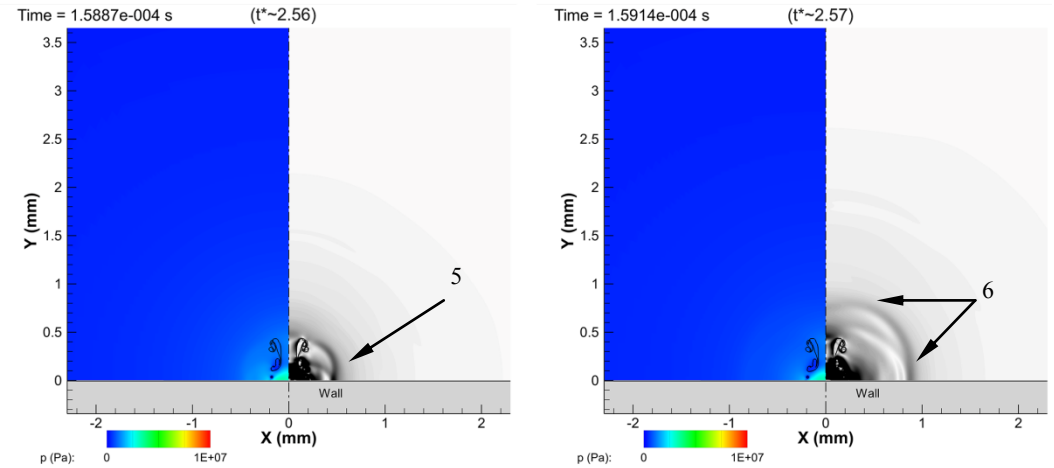

Figure 12. Left: pressure field. Right: Schlieren images during jet impact. The bubble has broken-up to two toroidal structures.

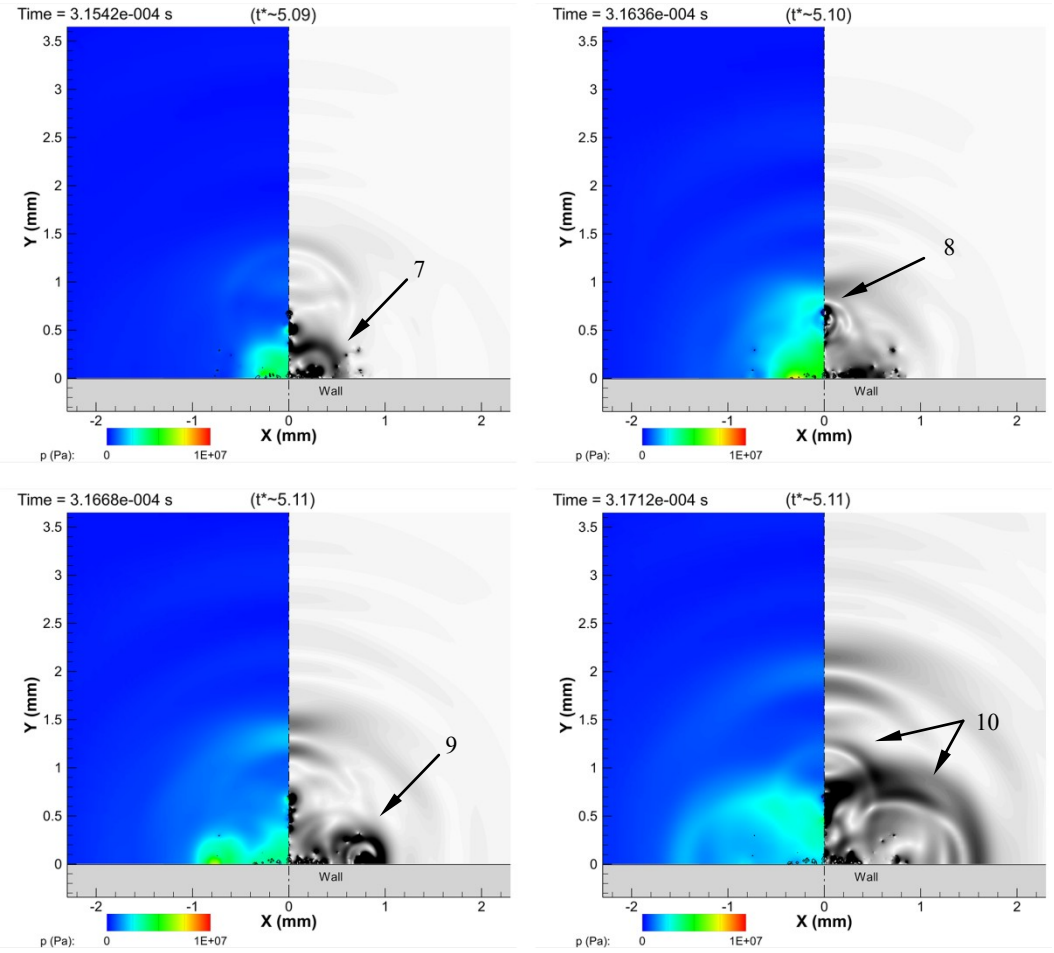

Figure 13. Left: pressure field. Right: Schlieren images during the second collapse.

The pressure signal away from the bubble was recorded during the experiment and it is directly comparable to simulation data, see Figure 14. The pressure signal is zero up to ~10 μs; then the spherical shock wave reaches the hydrophone (see *1* in Figure 14), raising locally the static pressure by 1.2 bar. It is reminded that the hydrophone is placed 15mm, or ~21.5 maximum bubble radii (R_{max} ~0.7), away from the bubble centre. After that, there are minor oscillations in the pressure signal, due to wave reflections, however, absolute pressure remains very close to atmospheric. The next notable pressure signal is at ~150-160 μs, after the first collapse of the bubble, see 2 in Figure 14. The peak over-pressure at this stage is ~ 0.5 bar and agrees well between the experiment and the simulation. Whereas the slope of the pressure signal matches between experiment and simulation, the exact time of the peak pressure is slightly shifted in the simulation, by ~ 7μs. After the first bubble collapse, the pressure signal becomes noisy, due to the multiple reflections of pressure waves on the irregular shape of the bubble. The next peak is found at ~250μs in the experiment and in the simulation at ~300μs; in both cases, the second peak is associated to the second bubble collapse, which is predicted later in the simulation in comparison to the experiment. Despite the discrepancy in the time, the pressure signal amplitude is still comparable even at the second collapse; the simulation predicts a peak overpressure of ~0.33bar, whereas in the experiment the peak overpressure is ~0.3bar.

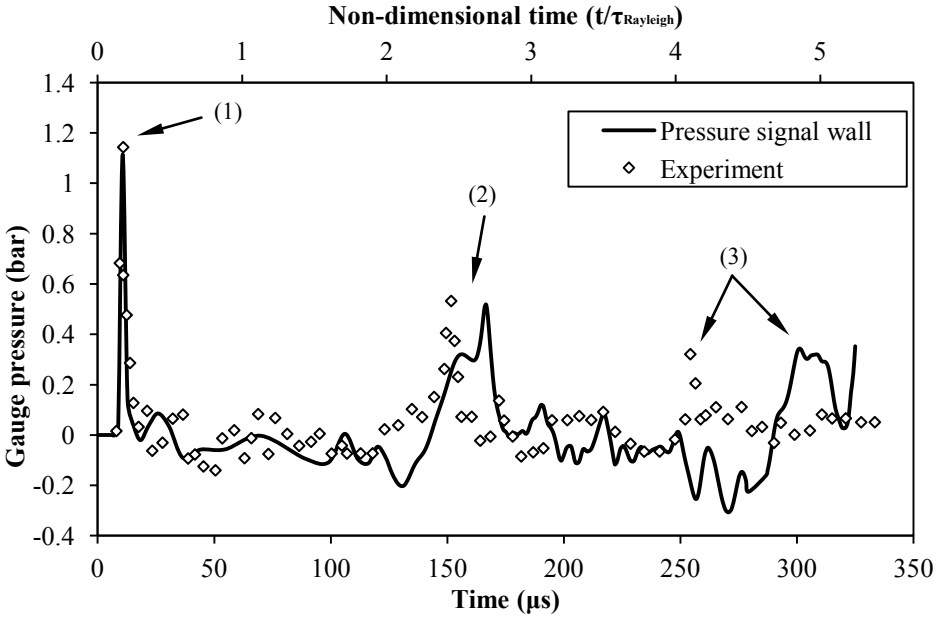

Figure 14. Pressure (gauge, i.e. relative to the atmospheric) signal at a distance of 15mm from the bubble generation site. Numbers indicate the respective phases of bubble evolution: (1) bubble generation, (2) first bubble collapse, (3) second bubble collapse. Non-dimensional time is expressed in terms of the Rayleigh collapse time ($\tau_{Rayleigh}$ = 62μs).

4.2. Shear stress measurement

In this section, the shear stress in the region of the stress transducer will be discussed. Since the actual transducer has finite dimensions and area (see Figure 1), averaging was performed to calculate the average shear stress on the surface area of the sensor. Averaging was performed after sampling the shear stress over time in the radial direction in the vicinity of the wall. As demonstrated in Figure 1, the placement of the transducer implies sampling over a span of radial distances, starting from 0.25mm up to 0.45mm. Note that the actual transducer cannot determine the flow direction [32,59], thus the absolute value of the wall shear stress was recorded from the simulation results to be comparable with the experiment. Since intense shearing of the bubble is observed (see e.g. Figure 8), variations of

density and laminar viscosity have been taken into account in the shear stress calculation, i.e. the fluid is not assumed to have constant liquid properties everywhere.

Experimental and numerical results of the evolution of the shear stress are shown in Figure 15a and numerical results of the parallel to the wall velocity ($u_{//}$ at 2.5μm from the wall) are shown in Figure 15b. The first recording of shear stress in the numerical results is at 0.42μs, peaking at value of ~1kPa; this is related to the induced flow by the initial shock wave emitted by the expanding bubble. As the bubble continues to expand at a reducing rate, shear stress gradually reduces to 0kPa at ~60μs. Then, as the bubble begins to collapse, shear stress increases again, up to 0.34kPa at ~147μs. In this interval the flow is reversed, as clearly demonstrated in Figure 15b, since the radial velocity is negative as liquid converges back to the bubble. At ~154μs there is a short drop in the shear stress, followed by a large peak, reaching up to 3kPa, see *2* in Figure 15a. The peak is associated with the high shear produced by the high speed liquid sheet, after the impact of micro-jet on the wall, see Figure 4 and Figure 5. Shear stress gradually reduces again, reaching zero at ~260μs when the bubbly structures reach maximum volume for the second time and then gradually increases again, due to flow reversal (see the negative velocity sign in Figure 15b, after 260μs). At the second collapse, a very high shear stress is observed, reaching ~5kPa; note that during the second collapse the bubbly structures are positioned much closer to the wall, in the vicinity of the stress sensor (see Figure 8), thus the induced flow is much stronger, see Figure 15b, where the parallel to the wall velocity reaches even 13m/s for the second collapse, compared to just 8m/s induced by the first collapse.

In general, experimental results show similar pattern to the numerical results, however some differences are observed. The experimental data do not show any sign of shear stress from 0 up to 150μs, i.e. till the first bubble collapse. Also, whereas experimental data show a high shear stress of ~3kPa at ~160μs corresponding to the first bubble collapse, there is not much evidence of shear stress induced by the second bubble collapse. According to the experimental data (see Figure 10), the second bubble collapse occurs at ~250μs. At this instant, only a minor peak (max. value ~0.29kPa) is observed in the measured shear stress. The simulation on the other hand predicts a delayed peak with significantly higher magnitude than the first one.

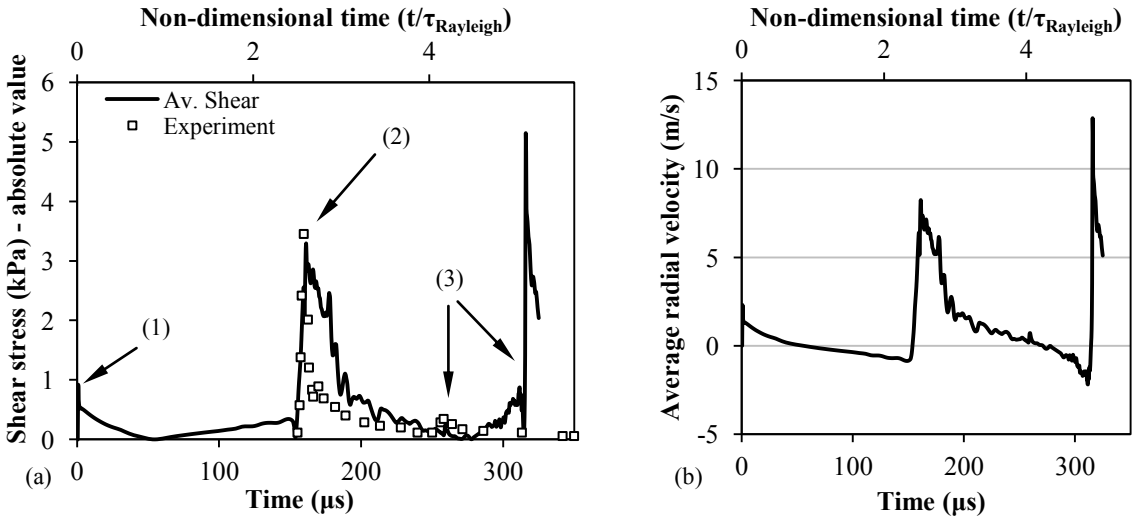

Figure 15. (a) Shear stress variation over time, for the sensor placement indicated in Figure 1; continuous line simulation, square marks experiment. (b) velocity parallel to the wall at a wall distance of 2.5μm. Numerical results are averaged over the equivalent sensor length.

The discrepancies observed are mainly related to two factors. The first one, concerning the numerical simulation, is the already discussed absence of condensation mechanism, which would reduce the amount of time needed for the second collapse and potentially its magnitude. The second

reason, related to the experimental measurements, has to do with the low sampling bandwidth [59] and the sensor calibration and type [32]. The sampling bandwidth of the sensor may lead to excessive smoothing of fast changes, which explains why the experimental signal is in general lower than the numerical one. The sensor type used is a heavy coating type, model 55R46, which is suitable for water. However, as demonstrated in Figure 8, the bubble after the first collapse is sheared across the wall surface. Indicatively, the simulation predicts that for radial distances 0.2 to 0.4mm, i.e. in the region of the sensor placement, gas volume fraction ranges between 0 to 100% (see Figure 16). This means that in reality the sensor may interact with gas/liquid mixture, instead of liquid water that was used for calibration and this could greatly affect the magnitude of the second shear stress peak.

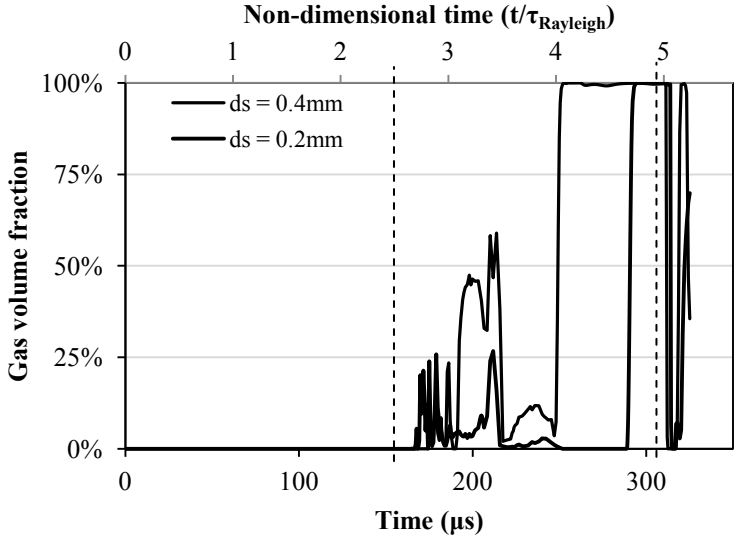

Figure 16. Gas volume fraction at the vicinity of the wall, for two indicative distances d_s from the bubble epicentre. Note that these distances correspond to the sensor location. The vertical dashed lines indicate the collapse time of the bubble.

4.4. Comparison of pressure and shear stresses on the wall surface

In this section, the induced shear stress and wall pressure are examined, in relation to the radial distance. Results are presented in Figure 17 and Figure 18 at various distances, d_s, from the bubble formation epicentre, starting from 0.2mm up to 1.2mm. The overall trend of shear stress point measurements is similar to the average shear stress recorded by the sensor, especially for the sampling points in the 1-1.2mm range. Sampling points closer to the bubble epicentre show a noisy shear stress over time, with variation from 1.5kPa (d_s = 1.2mm) up to even 36kPa (d_s = 0.2mm). A notable difference among the sampling points is the induced shear stress of the second bubble collapse, at ~314μs; for d_s = 0.2mm, the induced shear stress is towards the axis of symmetry, whereas for all the other sampling points it is towards the opposite direction, away from the axis of symmetry. This is directly related to the expansion of the bubble near the wall and its consequent compression against the wall, see Figure 8.

Minimum and maximum shear stress variation over the distance, d_s, resembles an inverse square variation, see Figure 15, both as averaged and point measurements, which is similar to published experimental results for large radii (non-dimensional radius $d_s/R_{jet} > 4$, see [60], [61]). Note that the variation is non-monotonic, i.e. when considering the induced shear stress of a jet on the wall, shear stress is zero at the stagnation point, then increases up to a maximum at $d_s/R_{jet} \sim 2$ and then decreases, however sampling was not performed at distances $d_s/R_{jet} < 2$.

The pressure field on the wall has also a similar pattern as the hydrophone signal, though the pressure pulse amplitude is much larger, since the measurement is conducted much closer to the bubble.

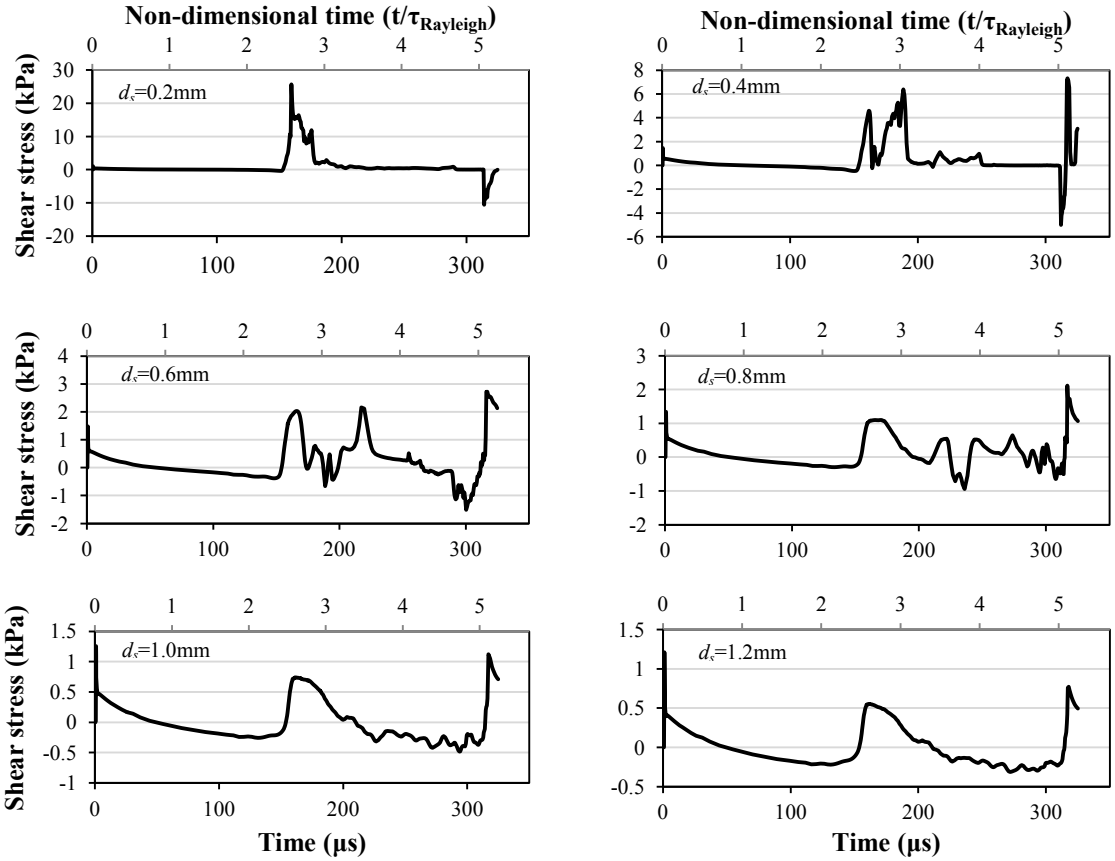

Figure 17. Shear stress variation across the wall, starting at d_s = 0.2mm up to 1.2mm from the bubble epicentre. Point measurements.

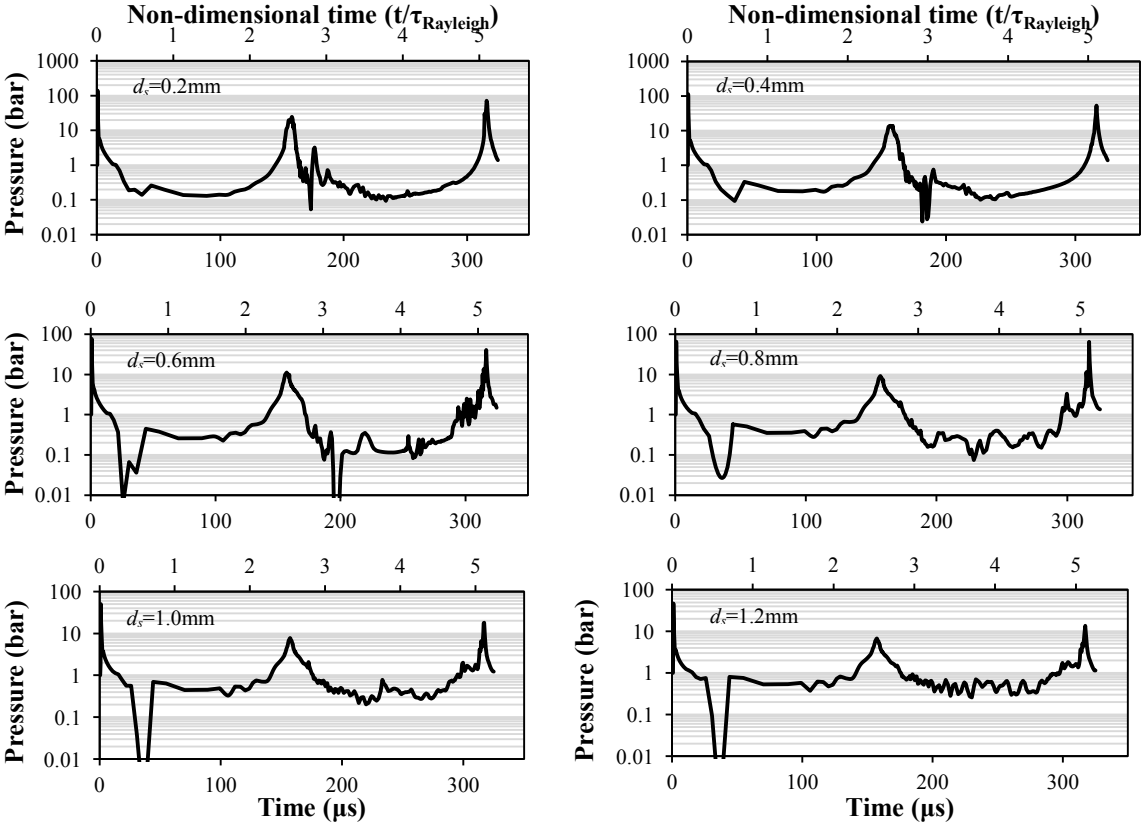

Figure 18. Pressure variation across the wall, starting at d_s = 0.2mm up to 1.2mm from the bubble epicentre. Point measurements.

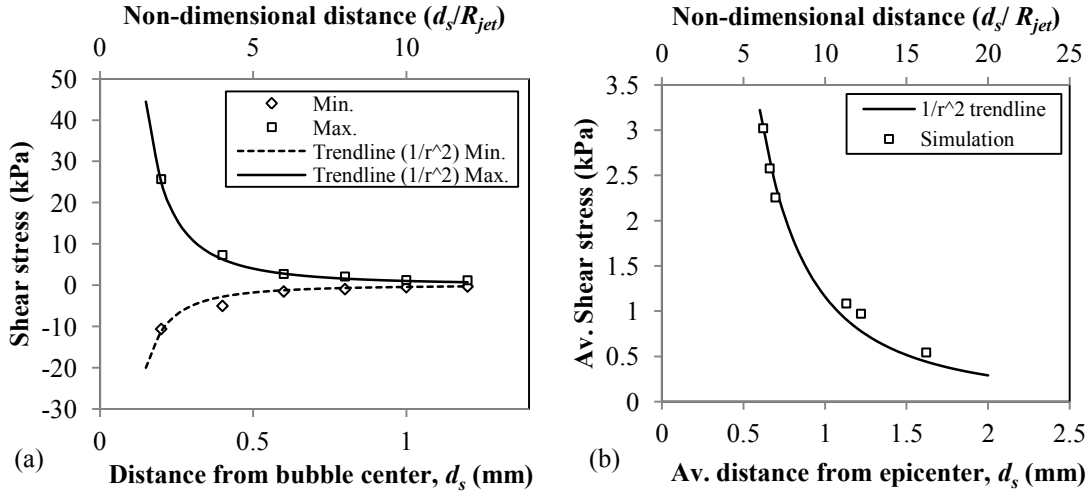

Figure 19. Shear stress dependence as a function of distance from the epicentre on the wall (symbols): (a) point measurements and (b) averaged (sensor) measurements. The inverse-square law trend line is provided as a comparison.

5. Parametric investigations

The last part of this investigation is to examine the effect of bubble distance from wall, h, and initial bubble pressure p_{g0} (which relates to the bubble energy, E_{bmax}) to the maximum induced shear stress. The cases examined have been summarized in Table 1 and the bubble volume over time is plotted in Figure 20. Volume evolution over time exhibits the well-known oscillating behaviour (collapse and rebound) for all cases. An observable difference between the cases involve the shorter oscillation period for lower initial pressures (cases *1*, *4*, *5*), which in turn results to smaller bubble sizes. Bubble to wall distance, h, has a weak influence on the volume evolution (cases *1*, *2*, *3*); in general all bubbles reached effectively the same maximum size, though during collapse there is an observable change in the minimum volume. It was noticed that the further a bubble is from the wall, the smaller its size during collapse. This is consistent with prior investigations relevant to collapse pressures [23] and luminescence [62-64], indicating that spherically symmetric collapses, which ideally are infinitely far from boundaries, reach the minimum size and achieve the highest compression.

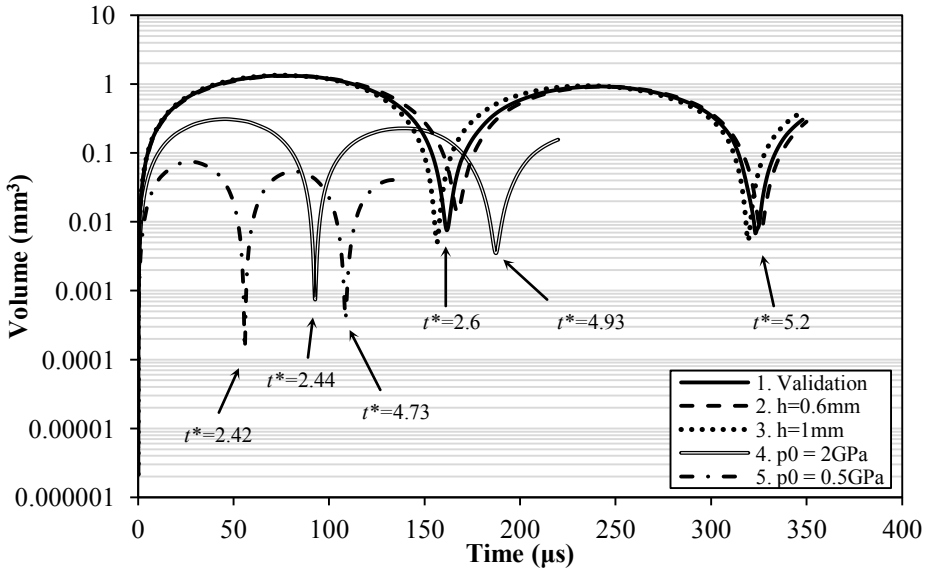

Figure 20. Bubble volume evolution for the discussed cases, as presented in Table 1. The non-dimensional time (t*=$t/\tau_{Rayleigh}$) is also provided at the instances of collapse.

Figure 21 summarizes the induced shear stress on the wall for all examined cases. The 3D graph shows the shear stress (z-axis) as a function of non-dimensional time, t^*, and measurement distance, d_s. Since the main interest of shear stress in cleaning applications is to dislocate dirt from wall surface, its exact direction is not relevant, thus the absolute value of the shear stress is used. Time is non-dimensionalized to keep the results in the same time scale.

The results indicate that the peak shear stress induced by the first bubble collapse is more or less the same for a given initial pressure, at least for the wall distances investigated, i.e. h ranging between 0.6 and 1mm. For example, peak values of shear stress are 28.9kPa (h = 0.6mm), 28.0kPa (h = 0.8mm) and 28.8kPa (h = 1mm) for an initial pressure of $8.5 \cdot 10^9$Pa. However, the area of effect of high shear is larger, when the bubble is closer to the wall, as becomes obvious from the width of the shear stress spike in Figure 21a, b, c. In particular, shear stresses higher or equal to 10kPa develop in a region of 0.277mm^2 for h = 0.6mm, 0.226mm^2 for h = 0.8mm, 0.050mm^2 for h = 1.0mm. Reduction of the initial pressure (and consequently the bubble energy) has a direct effect in the induced shear. Maximum shear stress appears to be a logarithmic function of bubble energy, i.e. it has a form $\tau_w = \alpha \cdot ln(E_b)+\beta$, assuming a constant bubble to wall distance h.

Concerning the second collapse, the correlation is more complicated. Among the bubbles of the same initial energy, but different bubble to wall distance, h, the one producing maximum shear stress is the one at $h \sim R_{max}$. Numerical results indicated that when the bubble is close to the wall ($h < R_{max}$), then, instead of splitting to two toroidal bubbles, it forms a single toroidal agglomeration which spreads over the wall surface. At the second collapse, this toroidal structure collapses mainly in the radial direction, converging towards the axis of symmetry and eventually directing the flow away from the wall, thus producing less shear than $h \sim R_{max}$. On the other hand, when the bubble is further away from the wall ($h > R_{max}$), the effect of the bubble collapse is smaller, due to the increased bubble to wall distance.

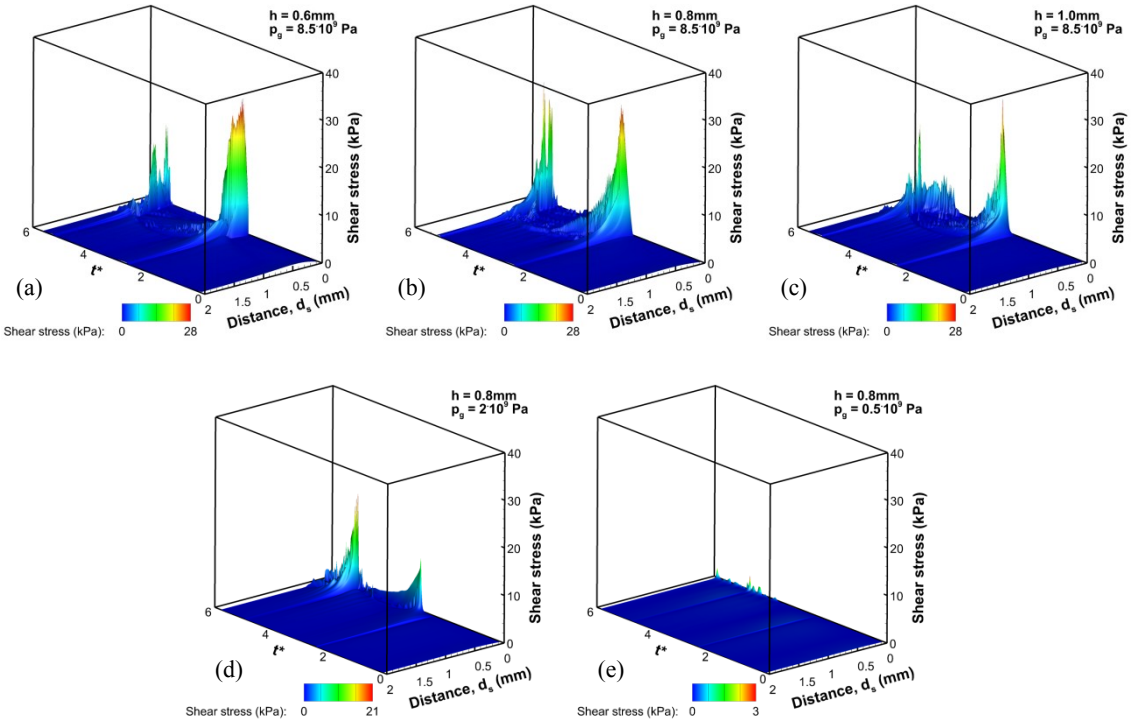

Figure 21. Absolute value of shear stress over non-dimensional time, t^* (= t / $\tau_{Rayleigh}$), along the distance, d_s, of the bubble epicentre to the measurement point. Time is non-dimensionalized according to the respective Rayleigh time, i.e.: (a), (b), (c) $\tau_{Rayleigh}$ = 62μs, (d) $\tau_{Rayleigh}$ = 38μs, (e) $\tau_{Rayleigh}$ = 23μs.

6. Conclusion

In this work, a numerical investigation of bubble collapses near wall has been performed, to determine the effect of bubble to wall and wall radial distance on the induced shear stress from the growth and collapse of a cavitation bubble. The investigation aims to complement and to provide further insight to prior experimental studies, oriented towards cleaning applications of cavitation bubbles.

The present investigation indicated that shear stress is produced by both the growth and the collapse of the bubble, though the most important contribution comes from the collapsing phase of the bubble. Indeed, during bubble collapse, microjet formation directs liquid at high velocity towards the wall. The liquid jet spreads as a thin, high-speed layer shearing over the wall surface.

Considering the different configurations examined, the bubble to wall distance did not alter significantly the maximum shear stress, the surface area exposed to high shear stress is inversely proportional to the distance though. On the other hand, the maximum shear was found to be related to the bubble energy as a logarithmic function.

Maximum shear is predicted to be produced at the first bubble collapse, after bubble generation. Subsequent collapses also produce shear, though the magnitude is decreased despite the fact that during the second collapse the bubble is closer to the wall than the first collapse. This is probably related to the irregular shape of the bubble after the rebound, which prevents efficient focusing of the liquid momentum towards the wall.

Acknowledgements

The research leading to these results has received funding from the People Programme (IAPP and IOP Marie Curie Actions) of the European Union's Seventh Framework Programme FP7/2007-2013/ under REA grant agreements n. 324313 and 329286. The authors would like to acknowledge the contribution of The Lloyd's Register Foundation. Lloyd's Register Foundation helps to protect life and property by supporting engineering-related education, public engagement and the application of research.

Nomenclature

ρ	Density (kg/m^3)
$\mathbf{u}$	Velocity vector field (m/s)
$\boldsymbol{\tau}$	Stress tensor (Pa)
$\mathbf{g}$	Acceleration of gravity (m/s^2)
$\mathbf{f}$	Body/volume forces vector (N/m^3)
μ	Dynamic viscosity (Pa·s)
λ	Bulk viscosity coefficient (Pa.s)
a	Gas volume fraction
n_l	Tait equation exponent (for liquid) (-)
ρ_0	Reference density (kg/m^3)
c_0	Reference speed of sound (m/s)
p_0	Reference pressure (Pa)
n	Polytropic exponent (for gas) (-)
k	Constant of polytropic gas process $\left(\frac{Pa}{\left(kg/m^3\right)^n} \right)$
c	Speed of sound (m/s)
ζ	Non-dimensional scaling law (-)
p_∞	Far-field pressure (Pa)
p_v	Vapour pressure (Pa)

h	Bubble-wall distance (m)
d_s	Distance from the bubble epicentre on the wall (m)
R	Bubble radius (m)
R_0	Initial bubble radius (m)
$\dot{R}$	Bubble interface velocity (m/s)
$\ddot{R}$	Bubble interface acceleration (m/s^2)
p_{g0}	Initial gas pressure (Pa)
σ	Surface tension (N/m)
Pe	Peclet number (-)
τ_{diff}	Thermal diffusion time scale (s)
τ_{dyn}	Dynamic time scale (s)
x_g	Gas thermal diffusivity (m^2/s)
k_g	Gas heat conductivity (W/m.k)
$c_{p,g}$	Gas heat capacity (J/kg.K)
$\tau_{Rayleigh}$	Rayleigh collapse time (s)

References

(1) Xu, S.; Qiao, Y.; Liu, X.; Church, C.; Wan, M. In *Cavitation in biomedicine: principles and techniques*; Wan, M., Feng, Y., ter Haar, G., Eds.; Springer Dordrecht, 2015.
(2) Rivas, D. F.;Taming acoustic cavitation. University of Twente, 2012.
(3) Rivas, D. F.; Verhaagen, B.; Seddon, J. R. T.; Zijlstra, A. G.; Jiang, L.-M.; van der Sluis, L. W. M.; Versluis, M.; Lohse, D.; Gardeniers, H. J. G. E. Localized removal of layers of metal, polymer, or biomaterial by ultrasound cavitation bubbles *Biomicrofluidics* **2012**, *6*.
(4) Kollath, A.; Andreeva, D. V. In *Food Preservation*; Academic Press: 2017, p 229.
(5) Tzanakis, I.; Lebon, G. S. B.; Eskin, D. G.; Pericleous, K. A. Characterisation of the ultrasonic acoustic spectrum and pressure field in aluminium melt with an advanced cavitometer *Journal of Materials Processing Technology* **2016**, *229*, 582.
(6) Weinberg, K.; Ortiz, M. Kidney damage in extracorporeal shock wave lithotripsy: a numerical approach for different shock profiles *Biomechanics and Modeling in Mechanobiology* **2009**, *8*, 285.
(7) Haar, G. T.; Coussios, C.-C. High intensity focused ultrasound: Physical principles and devices *International Journal of Hyperthermia* **2007**, *23*, 89.
(8) Hu, Y.; Wan, J.; Yu, A. Membrane perforation and recovery dynamics in microbubble-ediated sonoporation *Ultrasound Medical Biology* **2013**, *39*, 13.
(9) Duvshani-Eshet, M.; Baruch, L.; Kesselman, E.; Shimoni, E.; Machluf, M. Therapeutic ultrasound-mediated DNA to cell and nucleus: bioeffects revealed by confocal and atomic force microscopy *Gene Therapy* **2005**, *13*, 163.
(10) Wu, J.; Ross, J. P.; Chiu, J.-F. Reparable sonoporation generated by microstreaming *Journal of Acoustic Society Americas* **2002**, *111*, 1460.
(11) Ensminger, D.; Stulen, F. B. *Ultrasonics: Data, Equations and Their Practical Uses*; CRC Press, 2008.
(12) Awad, S. In *Ultrasound Technologies for Food and Bioprocessing*; Feng, H., Barbosa, G., Weiss, J., Eds.; Springer-Verlag: New York, 2011.
(13) Rivas, F. D.; Prosperetti, A.; Zijlstra, A. G.; Lohse, D. Efficient Sonochemistry through Microbubbles Generated with Micromachined Surfaces *Angewandte Chemie International Edition* **2010**, *49*, 9699.
(14) Verhaagen, B.; Liu, Y.; Galdames Perez, A.; Castro-Hernandez, E.; Rivas, F. D. Scaled–up sonochemical microreactor with increased efficiency and reproducibility *Chemistry Select* **2016**, *1*, 136.
(15) Chahine, G.; Kapahi, A.; Choi, J.-K.; Hsiao, C.-T. Modeling of surface cleaning by cavitation bubble dynamics and collapse *Ultrasonics sonochemistry* **2016**, *29*.
(16) Bremond, N.; Arora, M.; Ohl, C.-D.; Lohse, D. Controlled Multibubble Surface Cavitation *Physical review letters* **2006**, *96*, 4.

(17) Plesset, M. S.; Chapman, R. B. Collapse of an initially spherical vapor cavity in the neighborhood of a solid boundary *Journal of Fluid Mechanics* **1971**, *47*, 283.
(18) Sauter, S.; Schwab, C. *Boundary Element Methods*; 1st ed.; Springer-Verlag Berlin Heidelberg, 2011.
(19) Fu, Z.; Popov, V. In *Boundary Elements and Other Mesh Reduction Methods XXXIII*; Brebbia, C. A., Popov, V., Eds. 2011; Vol. 52.
(20) López-Villa, A.; Zamudio, L. S.; Medina, A. In *Experimental and Computational Fluid Mechanics*; Klapp, J., Medina, A., Eds.; Springer International Publishing: Cham, 2014, p 17.
(21) Chahine, G. L. In *Advanced Experimental and Numerical Techniques for Cavitation Erosion Prediction*; 1st ed.; Kim, K.-H., Georges, C., Franc, J.-P., Karimi, A., Eds.; Springer Netherlands: 2014, p 123.
(22) Hawker, N. A.; Ventikos, Y. Interaction of a strong shockwave with a gas bubble in a liquid medium: a numerical study *Journal of Fluid Mechanics* **2012**, *701*, 55.
(23) Lauer, E.; Hu, X. Y.; Hickel, S.; Adams, N. A. Numerical modelling and investigation of symmetric and asymmetric cavitation bubble dynamics *Computers & Fluids* **2012**, *69*, 1.
(24) Koch, M.; Lechner, C.; Reuter, F.; Köhler, K.; Mettin, R.; Lauterborn, W. Numerical modeling of laser generated cavitation bubbles with the finite volume and volume of fluid method, using OpenFOAM *Computers & Fluids* **2016**, *126*, 71.
(25) Koukouvinis, P.; Gavaises, M.; Supponen, O.; Farhat, M. Simulation of bubble expansion and collapse in the vicinity of a free surface *Physics of Fluids* **2016**, *28*, 052103.
(26) Koukouvinis, P.; Gavaises, M.; Supponen, O.; Farhat, M. Numerical simulation of a collapsing bubble subject to gravity *Physics of Fluids* **2016**, *28*, 032110.
(27) Franc, J.-P.; Michel, J.-M. *Fundamentals of Cavitation*; Kluwer Academic Publishers, 2005.
(28) Bremond, N.; Arora, M.; Ohl, C.-D.; Lohse, D. Cavitation on surfaces *Journal of Physics: Condensed Matter* **2005**, *2005*, 3603.
(29) Reuter, F.; Mettin, R.; Lauterborn, W. In *NAG - DAGA 2009 International Conference on Acoustics*; Boone, M. M., Ed.; Deutsche Gesellschaft für Akustik e.V. (DEGA): Rotterdam, 2009, p 1703.
(30) Reuter, F.; Mettin, R.; Lauterborn, W. In *Fortschritte der Akustik - DAGA 2010 Berlin*; Möser, M., Schulte-Fortkamp, B., Ochmann, M., Eds.; Deutsche Gesellschaft für Akustik e.V. (DEGA), Berlin: Berlin, 2010, p 677.
(31) Thiemann, A.; Nowak, T.; Mettin, R.; Holsteyns, F.; F., H.; Lippert, A. Characterization of an acoustic cavitation bubble structure at 230 kHz *Ultra Clean Processing of Semiconductor Surfaces IX, Solid State Phenomena* **2009**, *145-146*, 11.
(32) Dijkink, R.; Ohl, C.-D. Measurement of cavitation induced wall shear stress *Applied Physics Letters* **2008**, *93*, 4.
(33) Dijkink, R.;Confined cavitation: an experimental study. University of Twente, 2009.
(34) Malalasekera, W.; Versteeg, H. *An Introduction to Computational Fluid Dynamics: The Finite Volume Method* 2nd ed.; Prentice Hall, 2007.
(35) Moukalled, F.; Mangani, L.; Darwish, M. *The Finite Volume Method in Computational Fluid Dynamics: An introduction with OpenFOAM and Matlab*; Springer International Publishing, 2015; Vol. 113.
(36) Landau, L. D.; Lifshitz, E. M. *Fluid Mechanics*; 2nd ed.; Pergamon Press, 1987 Vol. 6.
(37) Chorin, A.; Marsden, J. *A Mathematical Introduction to Fluid Mechanics*; 3rd ed.; Springer, 2000.
(38) Batchelor, G. K. *An Introduction to Fluid Dynamics* Cambridge University Press, 2000.
(39) Holmes, M. J.; Parker, N. G.; Povey, M. J. W. Temperature dependence of bulk viscosity in water using acoustic spectroscopy *Journal of Physics: Conference Series, Anglo-French Physical Acoustics Conference* **2010**, *269 012011*.
(40) Brackbill, J. U.; Kothe, D. B.; Zemach, C. A continuum method for modeling surface tension *Journal of Computational Physics* **1992**, *100*, 335.
(41) Prosperetti, A.; Tryggvason, G. *Computational Methods for Multiphase Flow*; Cambridge University Press, 2009.
(42) Ivings, M. J.; Causon, D. M.; Toro, E. F. On Riemann solvers for compressible liquids *International Numerical Methods for Fluids* **1998**, *28*, 395.

(43) Wagner, W.; Kretzschmar, H.-J. *International Steam Tables - Properties of Water and Steam based on the Industrial Formulation IAPWS-IF97*; 2nd ed.; Springer-Verlag Berlin Heidelberg, 2008.
(44) Osterman, A.; Dular, M.; Sirok, B. Numerical simulation of a near-wall bubble collapse in an ultrasonic-field *Journal of Fluid Science and Technology* **2009**, *4*, 210.
(45) Toro, E. *Riemann Solvers and Numerical Methods for Fluid Dynamics: A Practical Introduction*; Springer-Verlag Berlin Heidelberg, 2009.
(46) Demirdžić, I.; Lilek, Ž.; Perić, M. A collocated finite volume method for predicting flows at all speeds *International Journal for Numerical Methods in Fluids* **1993**, *16*, 1029.
(47) *ANSYS Inc. Fluent 16.1 manual,* 2015
(48) Gopala, V.; van Wachem, B. Volume of fluid methods for immiscible-fluid and free-surface flows *Chemical Engineering Journal* **2008**, *141*, 204.
(49) Lauterborn, W.; Bolle, H. Experimental investigations of cavitation-bubble collapse in the neighbourhood of a solid boundary *Journal of Fluid Mechanics* **1975**, *72*, 391.
(50) Obreschkow, D.; Tinguely, M.; Dorsaz, N.; Kobel, P.; Bosset, A.; Farhat, M. A Universal Scaling Law for Jets of Collapsing Bubbles *Physical Review Letters* **2011**, *107*.
(51) Obreschkow, D.; Tinguely, M.; Dorsaz, N.; Kobel, P.; de Bosset, A.; Farhat, M. The Quest for the Most Spherical Bubble *Experiments in Fluids* **2013**, *54*.
(52) Louisnard, O.; González-García, J. In *Ultrasound Technologies for Food and Bioprocessing*; Feng, H., Barbosa-Canovas, G., Weiss, J., Eds.; Springer New York: New York, 2011.
(53) Leighton, T. G. *The Acoustic Bubble*; Academic Press, 1994.
(54) *NIST Standard Reference Database 23: Reference Fluid Thermodynamic and Transport Properties-REFPROP, Version 9.1,* Lemmon, E. W.; Huber, M. L.; McLinden, M. O. 2013
(55) Koukouvinis, P.; Gavaises, M.; Georgoulas, A.; Marengo, M. Compressible simulations of bubble dynamics with central-upwind schemes *International Journal of Computational Fluid Dynamics* **2016**, *30*, 129.
(56) Didden, N.; Ho, C.-M. Unsteady separation in a boundary layer produced by an impinging jet *Journal of Fluid Mechanics* **2006**, *160*, 235.
(57) Harvey, J. K.; Perry, F. J. Flowfield produced by trailing vortices in the vicinity of the ground *AIAA Journal* **1971**, *9*, 1659.
(58) Wu, M.; Martin, M. P. Direct Numerical Simulation of Supersonic Turbulent Boundary Layer over a Compression Ramp *AIAA Journal* **2007**, *45*, 879.
(59) Dantec Dynamics, Hot-wire and hot-film probes: technical reference, Single-sensor Film Probes, Model: 55R46
(60) Bradshaw, P.; Love, E. The normal impingement of a circular air jet on a flat surface *Reports and Memoranda* **1961**, *3205*.
(61) Phares, D. J.; Smedley, G. T.; Flagan, R. C. The wall shear stress produced by the normal impingement of a jet on a flat surface *Journal of Fluid Mechanics* **2000**, *418*, 351.
(62) Tinguely, M.;The effect of pressure gradient on the collapse of cavitation bubbles in normal and reduced gravity. Ecole Polytechnique Federale de Lausanne, 2013.
(63) Ohl, C.-D. Probing luminescence from nonspherical bubble collapse *Physics of Fluids* **2002**, *14*, 2700.
(64) Ohl, C. D.; Lindau, O.; Lauterborn, W. Luminescence from Spherically and Aspherically Collapsing Laser Induced Bubbles *Physical Review Letters* **1998**, *80*, 393.

Table of Contents

Cavitation bubbles located near walls collapse in a non-symmetric way, giving rise to jetting phenomena. This mechanism is one of the causes of cavitation erosion, but is exploited in applications of ultrasound cleaning. In this work, the shear stress distribution and pressure signal emissions have been investigated during the expansion and collapse of a laser-generated bubble in the vicinity of a wall. Moreover, a parametric investigation is performed to correlate the bubble energy and the bubble stand-off distance from the wall to the induced shear. The images show: (a) representation of the shock wave and jet during the collapse of the bubble (b) pressure signal in comparison to experiments (c) shear induced by the jet; results are compared to experiments (hydrophone and Constant Temperature Anemometry shear stress measurement). The present work contributes towards a better understanding of the cleaning mechanisms in ultrasound cleaning applications.